Brian A. Edge[1]
e-mail: bae127@psu.edu

Eric G. Paterson
e-mail: eric-paterson@psu.edu

Computational Mechanics Division,
Applied Research Laboratory and Department of
Mechanical and Nuclear Engineering,
The Pennsylvania State University,
State College, PA 16804

Gary S. Settles
e-mail: gss2@psu.edu
Department of Mechanical and Nuclear
Engineering,
The Pennsylvania State University,
University Park, PA 16802

Computational Study of the Wake and Contaminant Transport of a Walking Human

The unsteady aerodynamic wake of a human is studied using a time-accurate computational fluid dynamics simulation. Transport of a scalar contaminant, which originates on the body, is also considered. An existing Reynolds-averaged Navier-Stokes solver is modified to include energy, scalar-transport, and thermal buoyancy effects. Structured overset grids are used to discretize the geometry and the flow field. Results indicate two distinct wake regions: an unsteady bluff-body wake behind the torso which is characterized by a mean recirculation zone, and a region of unsteady vortex shedding behind the legs which is dominated by a "jet" of air formed between the legs. A significant downwash occurs behind the body which has the effect of laterally spreading the lower portions of the wake. The magnitude of the scalar contaminant is shown to decay exponentially within the wake and is found to be highly dependent upon the source location.
[DOI: 10.1115/1.2013291]

1 Introduction

The aerodynamics of the human wake has received little attention in the engineering community. This work is intended to contribute to the physical understanding of the dynamics of the human wake using computational fluid dynamics simulations. The transport of a scalar contaminant from the surface of the body and the subsequent mixing by the wake is also studied. This information may be of interest to many areas of the engineering community such as homeland defense and cleanroom design, as well as the broader medical community. The current work focuses on the aerodynamic wake behind a simplified human form, neglecting the small scale details of the human body which tend to vary from person to person.

The flow about the human body can be classified as a bluff-body flow. Literature regarding bluff-body flows indicate that instabilities arising in the separating boundary layer will cause the wake to be unsteady [1–3]. Studies of three-dimensional bluff bodies, such as finite cylinders mounted on flat plates and the three-dimensional flow around tall buildings [4–7], can provide insight into the dynamics of the wake that may be expected from the human body. These studies indicate that a downwash occurs behind three-dimensional structures. The study of circular cylinders of various aspect ratios by Okamoto and Sunabashiri [4] show that cylinders with an aspect ratio of 3, which is similar to the human geometry of this study, will have a recirculation region extending four diameters downstream. Their results also show that a cylinder with an aspect ratio of 3 is at the transition between symmetric and anti symmetric vortex shedding. While the human form definitely differs from the geometries used in these studies, it is clear that we should expect a recirculation zone in the wake that is on the order of four body widths in length. No expectations regarding symmetric or anti symmetric vortex shedding can be drawn from the studies as our geometry is close to the aspect ratio associated with transition between these two modes.

The gap between the legs provides a significant geometrical difference with the three-dimensional bluff bodies studied in the literature. Several studies have been performed on two-dimensional circular cylinders in side-by-side configurations [8,9] which is similar to the two legs of our human model. These studies have identified three different regimes for the wake structure, with the first regime occurring when the cylinders are placed closely together. In a closely spaced configuration, the wake is similar to that of a single bluff body with a width equivalent to the two cylinders. This regime occurs for cylinder gaps of up to 20% of the cylinder diameters. Gap widths larger than 20% of the cylinder diameter are associated with the second regime and are characterized by individual wakes behind each cylinder. These wakes strongly effect one another until the gap width reaches 120% of the cylinder diamter. Gap widths greater than 120% of the diameter allow each cylinder to act as an independent bluff body, although some synchronization between the vortex streets was noted. These studies show us that the wake behind the legs, which have a gap width of 50% of the leg diameter, will likely behave similar to the wakes observed in the second regime of the previous studies. Each leg will likely have an independent wake that is heavily influenced by the neighboring wake. The actual

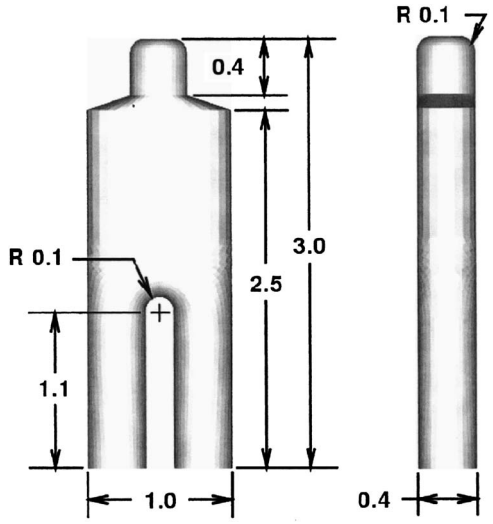

Fig. 1 Computational geometry shown with the nondimensional units (1.0 unit=0.58 m)

[1]Corresponding author.

Contributed by the Fluids Engineering Division for publication in the JOURNAL OF FLUIDS ENGINEERING. Manuscript received by the Fluids Engineering Division, November 11, 2004. Final Revision April 20, 2005. Associate Editor: Surya P Vanka.

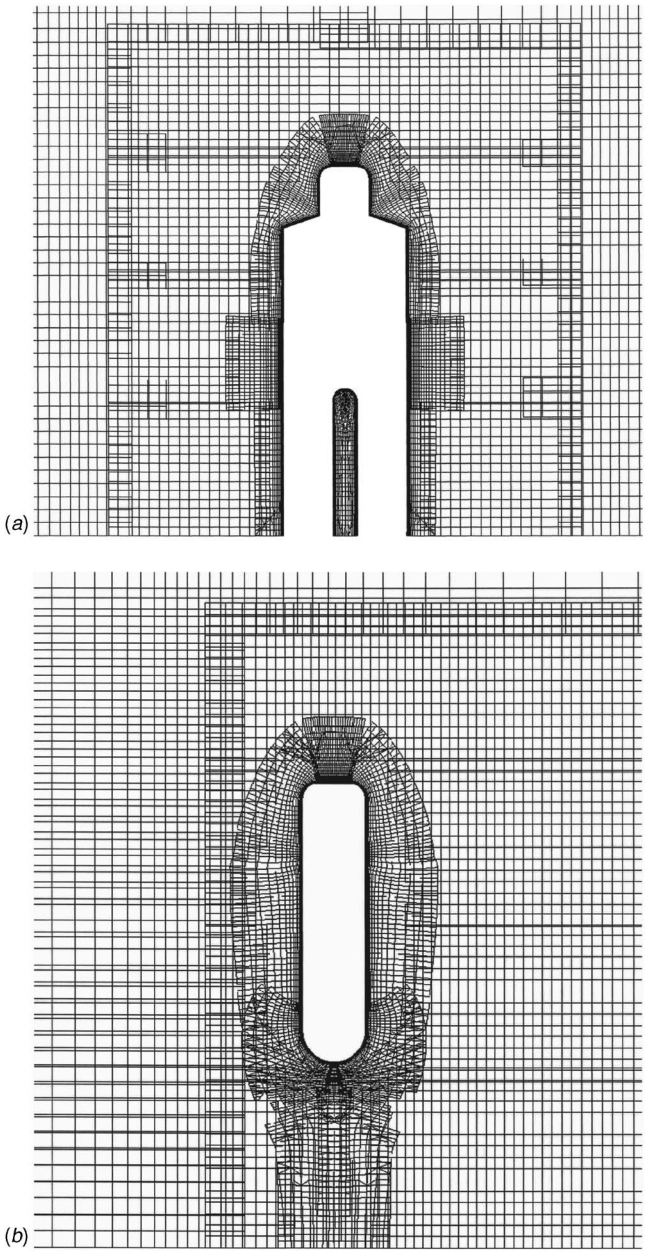

Fig. 2 Front (*a*) and side (*b*) details of the overset-grid system

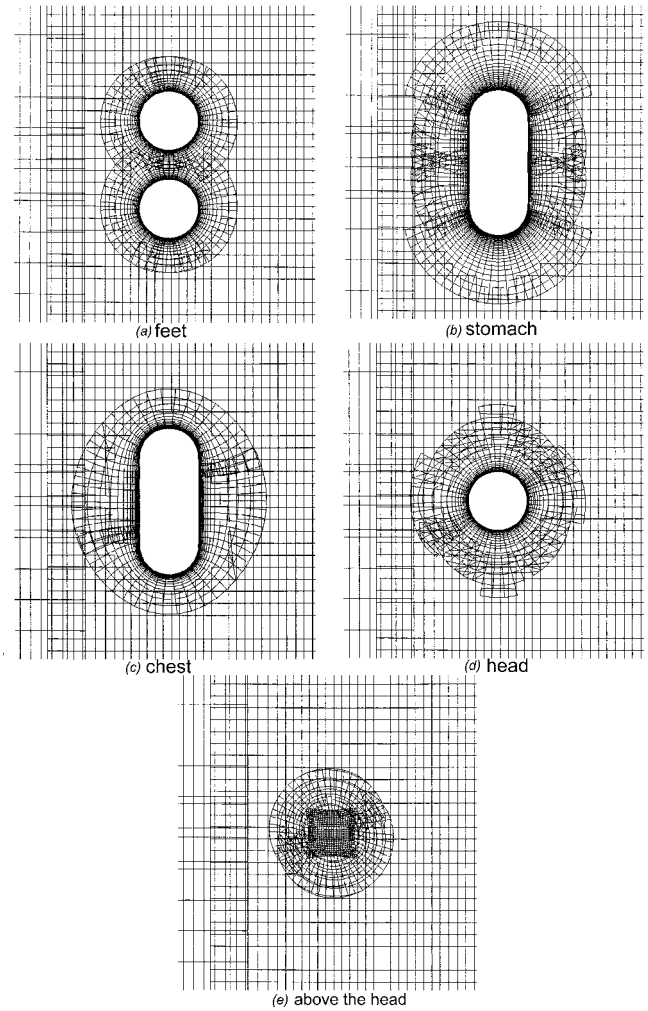

Fig. 3 Overset-grid layout: horizontal slices at various vertical elevations

behavior for this problem is difficult to determine in advance as the legs are not representative of the semi-infinite cylinders of the literature.

While the literature on bluff-body flows is quite numerous, there are also a few studies in the engineering literature regarding the human body. The flow about a stationary human in a quiescent environment was investigated decades ago by Lewis et al. [10] and Clark and colleagues [11,12], and more recently by Gowadia et al. [13], Settles and McGann; [14], Settles et al. [15], Gowadia and Settles [16], Gowadia [17], and Homma [18]. These works show the existence of a naturally occurring flow, known as the human thermal plume, with velocities of up to 1/4 m/s and volumetric flow rates of 50 l/s. When an external flow is combined with the buoyant human thermal plume, the relative importance of the buoyancy driven flow is deduced from the Richardson number Ri, which is the ratio of the Grashof number to the square of the Reynolds number, $\mathrm{Gr}/\mathrm{Re}^2$. The Reynolds number is defined as $\mathrm{Re}=U_0L/\nu$ where U_0 is the average velocity of the free stream flow, L is the characteristic length of the problem, and ν is the kinematic viscosity of the fluid. The Grashof number is $\mathrm{Gr}=g\beta\Delta TL^3/\nu^2$ where g is the gravitational constant, β is the volumetric thermal expansion coefficient, and ΔT is the temperature difference between the body and the free-stream air. When Ri is $\gg 1$, as it is for the human thermal plume, free convection dominates the flow. For a walking human, Re increases with walking speed which tends to reduce Ri. When Ri becomes much less than 1, forced convection dominates the flow and the free convection becomes negligible.

Research is quite limited for the aerodynamics of the human wake that develops under dominant external flow ($\mathrm{Ri}\ll 1$). Most studies of the human form have focused on thermal issues of the human body [19,18], measurement and prediction of the drag characteristic of a walking person [20], or lateral airflow studies motivated by air pollution control and reduction of worker exposure [21–23]. Murakami et al. [20] performed a three-dimensional steady-state computational simulation of the lateral flow about a human form under flow speeds of 0.25 and 2.5 m/s which correspond to Re (based upon body width) of 8×10^3 and 8×10^4, respectively. The authors, who were primarily focused upon predicting the thermal properties and drag, provide little discussion of the dynamics of the wake.

The human form used by Murakami et al. does not resolve separate legs with a gap between. While this geometry is quite acceptable for studies of lateral flow, ongoing experimental work

Table 1 Initial conditions and boundary conditions

Description	U	V	W	Φ	P	k	ω	ν_t
Initial conditions	0	0	0	0	0	10^{-7}	9.0	1.1
Inlet	1.0	0	0	0	0	1×10^{-7}	9.0	1.1×10^{-8}
Exit	$\frac{\partial^2 U}{\partial \xi_i^2}=0$	$\frac{\partial^2 V}{\partial \xi_i^2}=0$	$\frac{\partial^2 W}{\partial \xi_i^2}=0$	$\frac{\partial \Phi}{\partial \xi_i}=0$	$\frac{\partial P}{\partial \xi_i}=0$	$\frac{\partial k}{\partial \xi_i}=0$	$\frac{\partial \omega}{\partial \xi_i}=0$	$\frac{\partial \nu_t}{\partial \xi_i}=0$
Far-field	1.0	0	0	$\frac{\partial \Phi}{\partial \xi_i}=0$	$\frac{\partial P}{\partial \xi_i}=0$	$\frac{\partial k}{\partial \xi_i}=0$	$\frac{\partial \omega}{\partial \xi_i}=0$	$\frac{\partial \nu_t}{\partial \xi_i}=0$
Impermeable-slip, no force	See text	See text	See text	$\frac{\partial \Phi}{\partial \xi_i}=0$	$\frac{\partial P}{\partial \xi_i}=0$	$\frac{\partial k}{\partial \xi_i}=0$	$\frac{\partial \omega}{\partial \xi_i}=0$	$\frac{\partial \nu_t}{\partial \xi_i}=0$
No-slip	0	0	0	1	$\frac{\partial P}{\partial \xi_i}=0$	0	$\frac{60}{\mathrm{Re}\,0.075\Delta^2}$	0

by the Gas Dynamics Laboratory at The Pennsylvania State University indicates that the leg separation has a significant effect on the structure of the wake for flows in the primary walking direction [24]. This experimental work consisted of flow visualizations of the wake behind a walking person and measurement of the decay rate of a passive scalar originating from the surface of the human body. The Gas Dynamics Laboratory work shows the wake structure characterized by considerable intermittency at the boundaries and an obvious left-right vortex shedding which is characteristic of bluff-body wakes. The wake shows little lateral growth to a distance of about three body widths down-stream, followed by a quasilinear growth attributed to turbulent mixing. This work also indicates that the swinging of arms during walking has little significance in the formation of the wake. A passive scalar tracer, placed on the frontal midriff of a walking person, was found to decay rapidly in an exponential fashion.

The focus of the present work is to investigate the dynamics of the human wake and transport of a scalar surface contaminant using computational fluid dynamics simulation tools. This work involves the solution of the three-dimensional unsteady Reynolds-averaged Navier-Stokes equations with thermal buoyancy effects and scalar transport. The following sections will introduce the simplified human geometry, the governing equations, and the numerical methods that were used to solve the equations. A brief review of the computational uncertainty is presented, followed by results, conclusions, and recommendations for future work.

2 Model Equations

The flow about the human form is modeled with the nondimensional unsteady Reynolds-averaged Navier-Stokes (URANS) equations in the incompressible form.

$$\frac{\partial U_i}{\partial X_i}=0 \tag{1}$$

$$\frac{\partial U_i}{\partial t}+U_j\frac{\partial U_i}{\partial X_j}=-\frac{\partial P}{\partial X_i}+\left(\frac{1}{\mathrm{Re}}+\nu_t\right)\frac{\partial^2 U_i}{\partial X_j\,\partial X_j}+\frac{\partial \nu_t}{\partial X_j}\left(\frac{\partial U_i}{\partial X_j}+\frac{\partial U_j}{\partial X_i}\right)+\delta_{i3}\frac{\mathrm{Gr}}{\mathrm{Re}^2}\Theta \tag{2}$$

$$\frac{\partial \Theta}{\partial t}+U_i\frac{\partial \Theta}{\partial X_i}=\left(\frac{1}{\mathrm{Re\,Pr}}+\frac{\nu_t}{\mathrm{Pr}_t}\right)\frac{\partial^2 \Theta}{\partial X_j\,\partial X_j}+\frac{1}{\mathrm{Pr}_t}\frac{\partial \nu_t}{\partial X_j}\left(\frac{\partial U_i}{\partial X_j}+\frac{\partial U_j}{\partial X_i}\right)-\frac{2}{3}\frac{\partial k}{\partial X_i} \tag{3}$$

where the velocity terms are nondimensionalized by the free stream velocity ($U_i=u_i/U_0$), the Cartesian coordinates are nondimensionalized by the characteristic length ($X_i=x_i/L$), and the temperature values are nondimensionalized by the body temperature

$$\Theta=\frac{T(x,t)-T_\infty}{T_{\mathrm{body}}-T_\infty} \tag{4}$$

Pr is the Prandtl number defined as $\mathrm{Pr}=C_p\mu/k_t$ where C_p is the specific heat at constant pressure, μ is the dynamic viscosity, and k_t is the thermal conductivity. The contaminant is modeled using a scalar transport equation which assumes the mass and volume fractions are negligible, the contaminant is one-way coupled with the flow, and the contaminant has the same velocity as the local fluid. The contaminant is also assumed to have no effect on the turbulence in the carrier fluid.

$$\frac{\partial S}{\partial t}+U_i\frac{\partial S}{\partial X_i}=\left(\frac{1}{\mathrm{Re\,Sc}}+\frac{\nu_t}{\mathrm{Sc}_t}\right)\frac{\partial^2 S}{\partial X_j\,\partial X_j}+\frac{1}{\mathrm{Sc}_t}\frac{\partial \nu_t}{\partial X_j}\left(\frac{\partial U_i}{\partial X_j}+\frac{\partial U_j}{\partial X_i}\right)-\frac{2}{3}\frac{\partial k}{\partial X_i} \tag{5}$$

The Schmidt number, Sc is defined as $\mathrm{Sc}=\nu/D_{AB}$ where D_{AB} is

Table 2 Computational resources

Grid resolution	Number of blocks	Total points	Maximum points/block	Memory per processor (Mb)	Wall clock time per time step (s)
Fine	31	2.8 million	131,000	295	347
Intermediate	17	1 million	78,000	107 (est.)	60
Coarse	17	371,000	29,000	40 (est.)	11

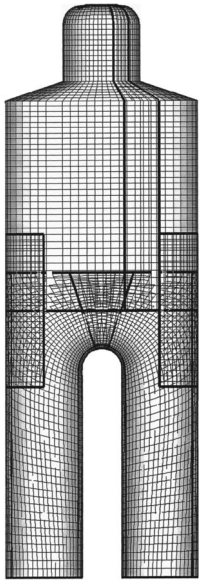

Fig. 4 Layout of the surface grids on the computational geometry

the mass diffusivity. The set of equations are closed by means of a linear stress-strain closure with an eddy viscosity computed by the two-equation blended k-ϵ/k-ω model of Menter [25]. While the k-ϵ model does a fine job predicting free stream turbulence quantities, the k-ω model has been shown to more accurately predict separation of boundary layer flows in adverse pressure gradients. Menter's model smoothly blends from the k-ω model near no-slip surfaces to the k-ϵ model in the free stream and wake.

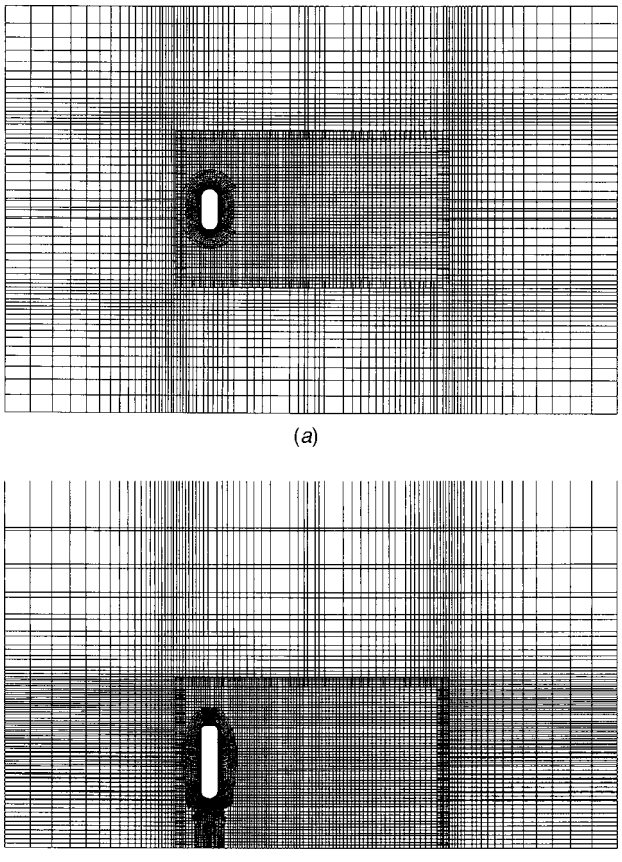

(*a*)

(*b*)

Fig. 5 Top (*a*) and side (*b*) views of the full overset-grid domain

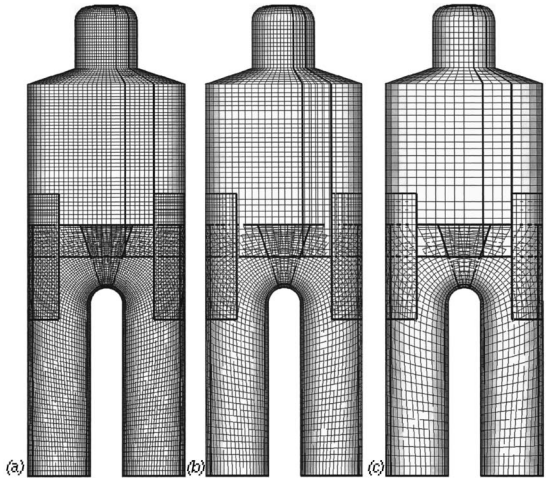

Fig. 6 a View of the fine (*a*), intermediate (*b*), and coarse (*c*) surface grids which were used in the grid refinement study

3 Geometry and Flow Conditions

The human body varies from person to person and can even change based upon the clothing worn. Considering all the variability, a simplified form, shown in Fig. 1, was chosen for this

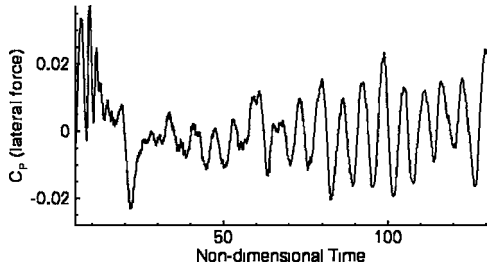

Fig. 7 Coefficient of pressure in the lateral direction versus nondimensional time as computed on the medium grid

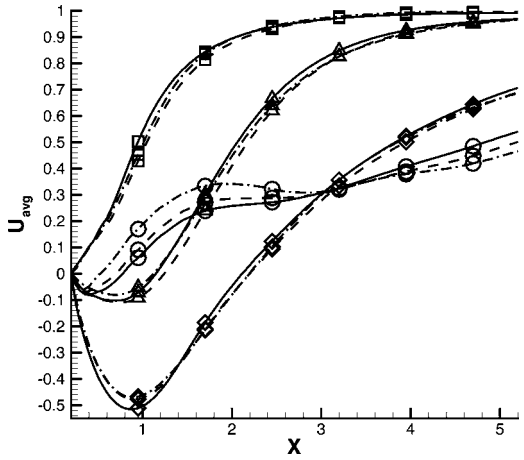

Fig. 8 Computed-mean *U* velocity for three different sample sizes versus downstream distance *X*. The line types define the sample set: — 150 time units, – – – 100 time units, and – - – 50 time units. The symbols define the location of the sample: □ head, △ chest, ◇ stomach, and ○ feet. U_{avg} is the nondimensional average velocity and *X* is the nondimensional distance downstream of the body.

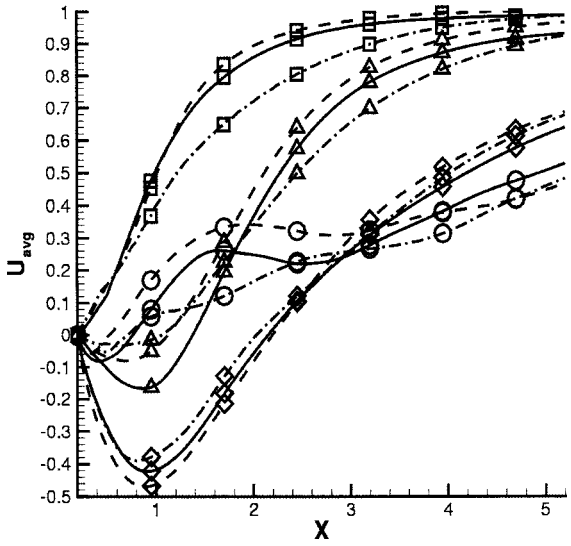

Fig. 9 Computed-mean *U* velocity of the three grid resolutions versus downstream distance at nondimensional time 50. The line types define the grid resolution: — fine grid, – – – medium grid, and – - – coarse grid. The symbols define the location of the sample: □ head, △ chest, ◇ stomach, ○ feet.

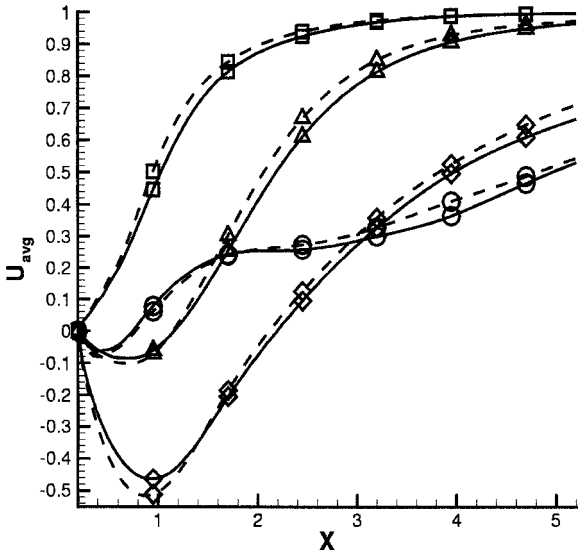

Fig. 11 Computed-mean *U* velocity at nondimensional time 50 for two different time step sizes. The line types represent the nondimensional time step size: — Δt=0.005, – – – Δt=0.01. The symbols represent the location of the sample: □ head, △ chest, ◇ stomach, and ○ feet.

computational work. The geometry is representative of a human with hands at the side and consists of a head, torso, and separate legs. The dimensions are derived from the human model used in the work of the Penn State Gas Dynamics Laboratory [24] and are nondimensionalized by the width of the shoulders (L=0.58 m).

The flow conditions are based upon a walking speed (U_0) of 1.34 m/s and a temperature difference between the body and the surrounding air of 10 K. This leads to Re=53,000 ($\nu=1.43\times10^{-5}$ m^2/s), and Gr=3.05×10^8 (g=9.81 m/s^2, β =0.0034 K^{-1}). The corresponding Ri of 0.109, indicates that the flow is dominated by forced convection. The flow is also assumed to have a Pr=0.693 [C_p=1.007 kJ/(kgK), $k=26\times10^{-3}$ W/(mK)] and Sc, for lack of experimental data, is assumed to have the same value as Pr.

4 Numerical Methods

Equations (1)–(5) are discretized in a grid-based coordinate system as outlined in Paterson et al. [26]. The temporal terms are discretized using the second-order backward difference for all but the first time step, where a first-order backward difference method is used. The spatial convective terms are discretized using a second-order upwind scheme while the diffusive terms are discretized using second-order accurate central-difference methods. The solver utilizes a segregated approach to the equations and handles the pressure and velocity coupling using the pressure-implicit with splitting of operators approach of Issa [27]. The Computational fluid dynamics code has been used and validated for many applications, e.g., complex bluff-body drag prediction [28], trailing-edge detached-eddy simulations [29], propulsion structural acoustics [30], jet cavitation [31], and Coanda-effect circulation control [32].

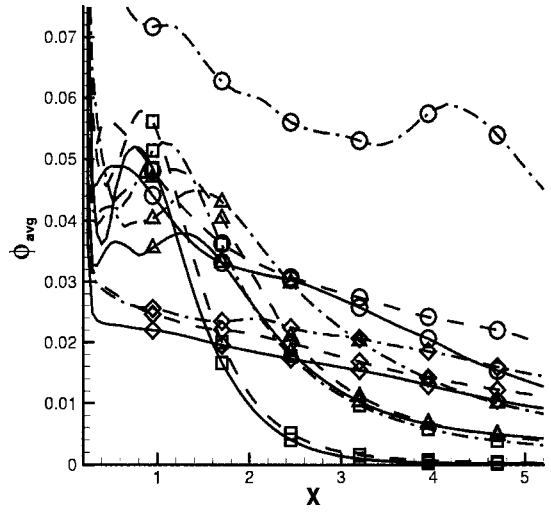

Fig. 10 Computed-mean scalar quantity for the three grid resolutions versus downstream distance at nondimensional time 50. The line types define the grid resolution: — fine grid, – – – medium grid, and – - – coarse grid. The symbols define the location of the sample: □ head △ chest, ◇ stomach, and ○ feet. The values of the computed-mean scalar quantities go to a limit of 1 at the body source *X*=0.

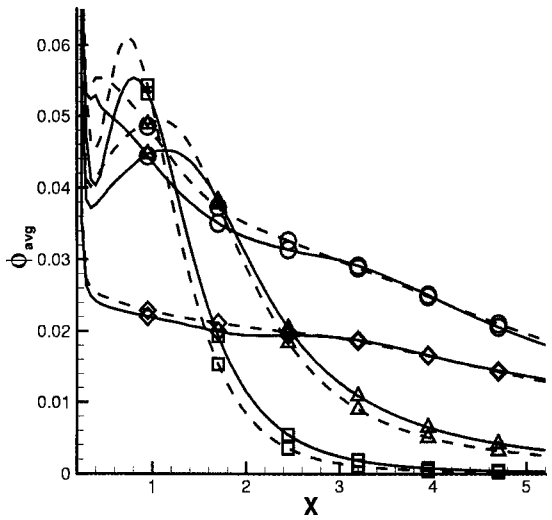

Fig. 12 Computed-mean scalar quantity at nondimensional time 50 for two different time step sizes. The line types represent the nondimensional time step size: — 0.005, and – – – Δt =0.01. The symbols represent the location of the sample: □ head, △ chest, ◇ stomach, and ○ feet.

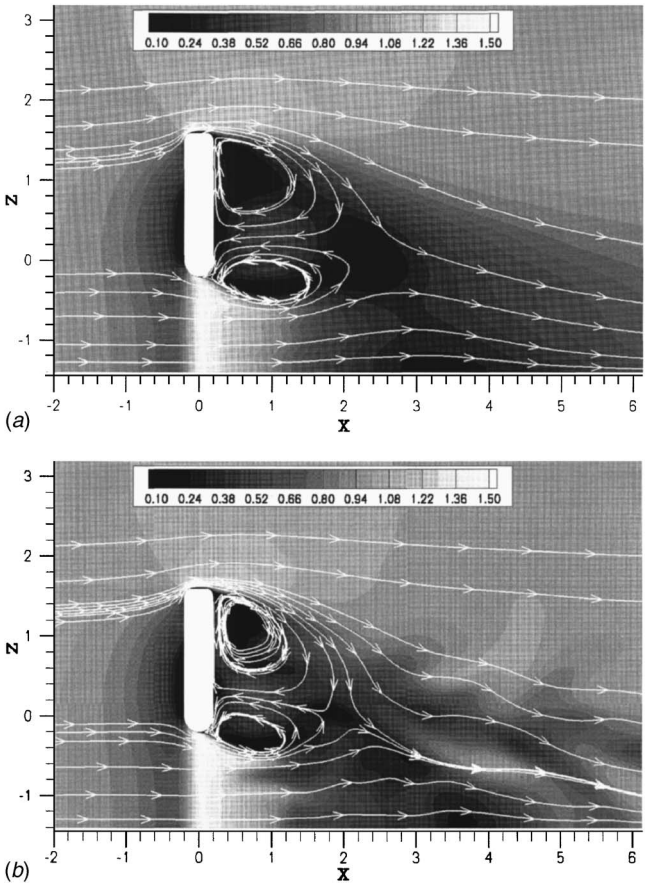

Fig. 13 Computed-mean (*a*) and instantaneous (*b*) total velocity magnitude with tangential streamlines in a vertical slice through the body centerline

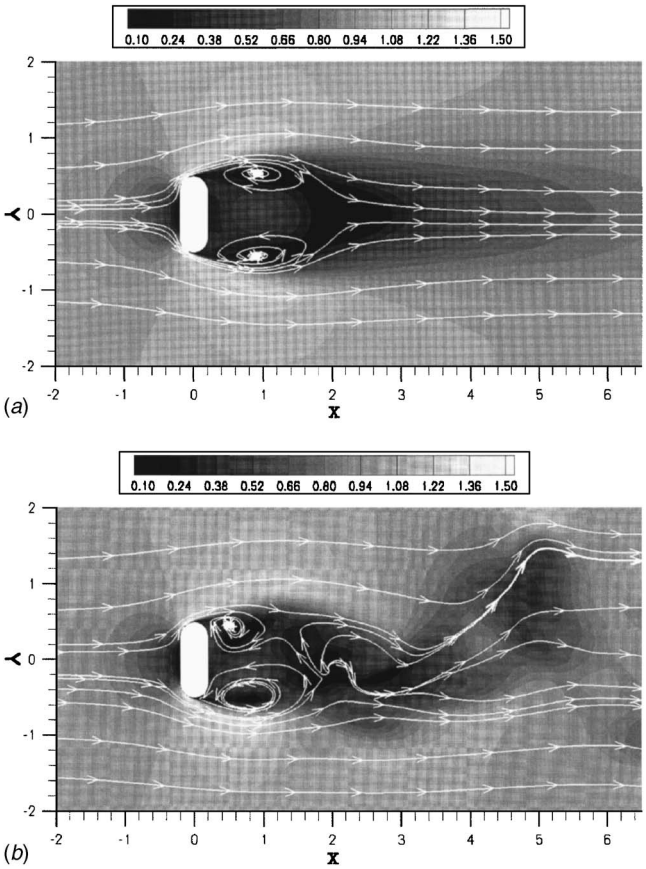

Fig. 14 Computed-mean (*a*) and instantaneous (*b*) total velocity magnitude with tangential streamlines in a horizontal slice through the stomach

The initial and boundary conditions for the dependent variables are listed in Table 1. The "impermeable-slip, no force" boundary condition is formulated using contravariant velocity components at one point off the boundary where the tangential components are computed assuming zero stress and the normal component is set to zero. This boundary condition is used on the bottom surface of the domain to approximate the ground below a walking person. Note that Δ, in the equation for ω, is defined as the distance to the first grid point off the no-slip surface. More details regarding the formulation of the boundary conditions can be found in Paterson et al. [26].

5 Grid Generation

The computational domain is an assembly of structured overset grids which are shown in Figures 2 and 3 [33,34]. The surface grids on the body, shown in Fig. 4, are extruded hyperbolically from the surface with an initial grid spacing of 1.43×10^{-4}, which corresponds to a y^+ value of less than 1. The y^+ term represents the viscous length and is defined as $y^+=u_\tau y/\nu$ where y is the dimensional distance to the wall, ν is the kinematic viscosity, and u_τ is the friction velocity defined as $u_\tau=\sqrt{\tau_w/\rho}$, where τ_w is the wall shear stress and ρ is the density [35]. Placing the first grid point at $y^+\leqslant 1.0$ ensures a sufficient number of grid points within the buffer layer, where turbulent production rapidly increases. This also ensures that the total number of grid points within the boundary layer are between 15 and 20 for these simulations.

The far-field boundaries are placed 4.8 units upstream, 4.5 units to the side, and 9.8 units downstream (one unit corresponds to the width of the body). The full domain is shown in Fig. 5. Notice the use of nested box grids, shown clearly in Fig. 5, to provide greater resolution in the near-wake regions of the flow.

Three different grid resolutions, depicted in Fig. 6, were used for a grid refinement study. The intermediate grid was generated from the fine grid by using linear interpolation to increase the grid spacing by a factor of $\sqrt{2}$ in all grid directions. The coarse grid is generated from the intermediate grid in the same manner. Table 2 lists the physical and computational sizes of each grid, where we see that the finest grid consists of more blocks than either the intermediate or coarse grids. This is a result of splitting the largest blocks for load balancing during parallel computations. The computer resource requirements are based upon an IBM SP system with 1024 Power3 processors running at 375 MHz. The computational fluid dynamics code is parallelized using the message passing interface standard which allows each individual block to be computed on a dedicated CPU.

6 Numerical Uncertainty

Numerical uncertainty is investigated through the comparison of results from three systematically refined grids and two different time step sizes. As the flow is naturally unsteady, the computed-mean quantities of the flow are used as the verification metrics. This method of comparison is not without difficulties since the exact mean quantities can only be obtained in the limit of an infinite sample. We can therefore expect the computed-mean to contain numerical sampling errors which can only be reduced by collecting a sample that is substantially longer than the lowest frequency fluctuations in the flow field, or by capturing an exact integer value of the fluctuations (assuming that they are repeating fluctuations, which is unlikely for a nonlinear problem with multiple length scales). Reducing the error to a value that is very

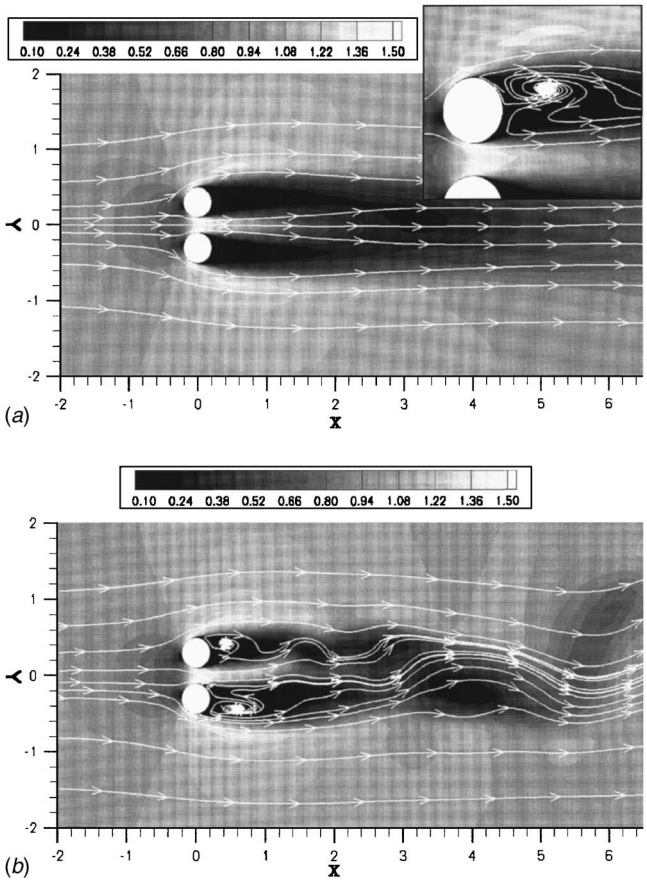

Fig. 15 Computed-mean (*a*) and instantaneous (*b*) total velocity magnitude with tangential streamlines in a horizontal slice through the ankles

small in comparison with the signal is quite expensive for these naturally unsteady flows, especially in regions where the mean velocity is small compared with the fluctuations.

The unsteady flow is started from a zero velocity field and a transient period exists where the flow transitions to the quasisteady, or stationary, flow state. Figure 7 shows the time history of the integrated surface pressure force coefficient C_p associated with lateral forces (i.e., perpendicular to the walking direction). This figure indicates that the solution does not reach its quasisteady state values until after a nondimensional time of 50. Ideally, the

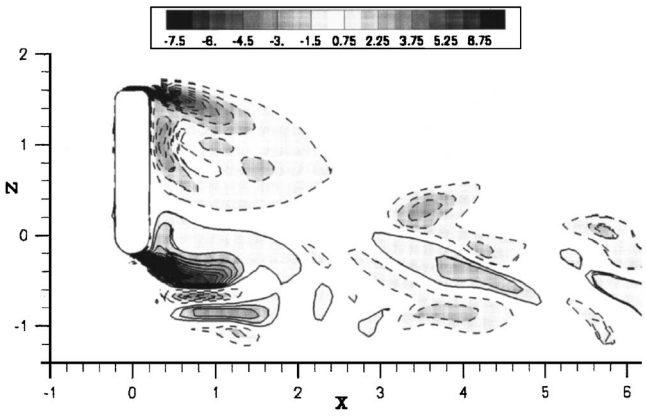

Fig. 16 Instantaneous vorticity for a vertical slice through the body centerline. Positive vorticity is bounded by solid lines and negative vorticity is bounded by dashed lines.

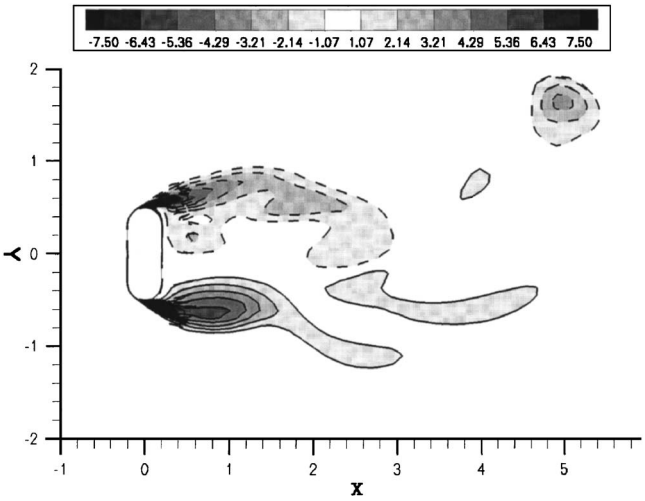

Fig. 17 Instantaneous vorticity for a horizontal slice through the stomach. Positive vorticity is bounded by solid lines and negative vorticity is bounded by dashed lines.

computed-mean sampling would begin after this point, however the computational expense associated with this simulation made it prohibitively expensive to rerun the simulations after obtaining this information. All time-averaged quantities presented in this paper represent samples taken from a starting time of zero through the specified ending time.

The computational expense for the finest grid is also substantial, requiring almost 350 (s) per time step. The computed-mean quantities from this grid are based upon a sample collected over a nondimensional time of 50, whereas the computed-mean samples from the other grids were collected over a nondimensional time of 150. Although the quasisteady state has not been reached for the body forces, some portions of the flow field have reached a quasisteady state as seen in Fig. 8. The computed-mean U velocity at several locations in the wake of the body are compared at nondimensional times of 50, 100, and 150. Figure 8 shows that the computed-mean solutions behind the head, chest, and stomach show little change between the 50, 100, and 150 time unit samples, whereas the solution behind the lower portion of the wake shows some variation. It is reasonable to conclude that the present grid study, which compares the time-averaged solutions for the upper wake, will provide reasonable assurances that grid convergence has been reached.

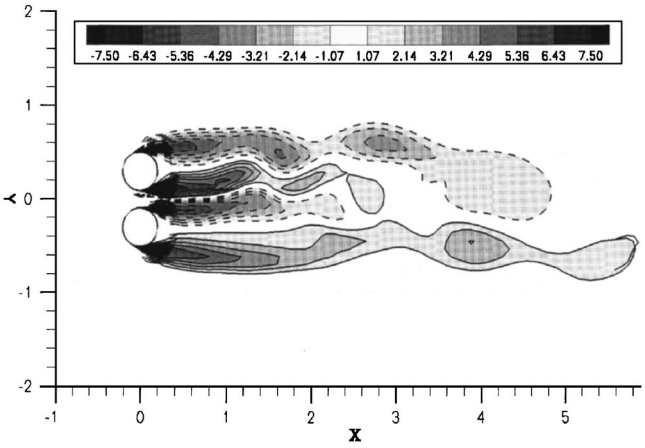

Fig. 18 Instantaneous vorticity for a horizontal slice through the ankles. Positive vorticity is bounded by solid lines and negative vorticity is bounded by dashed lines.

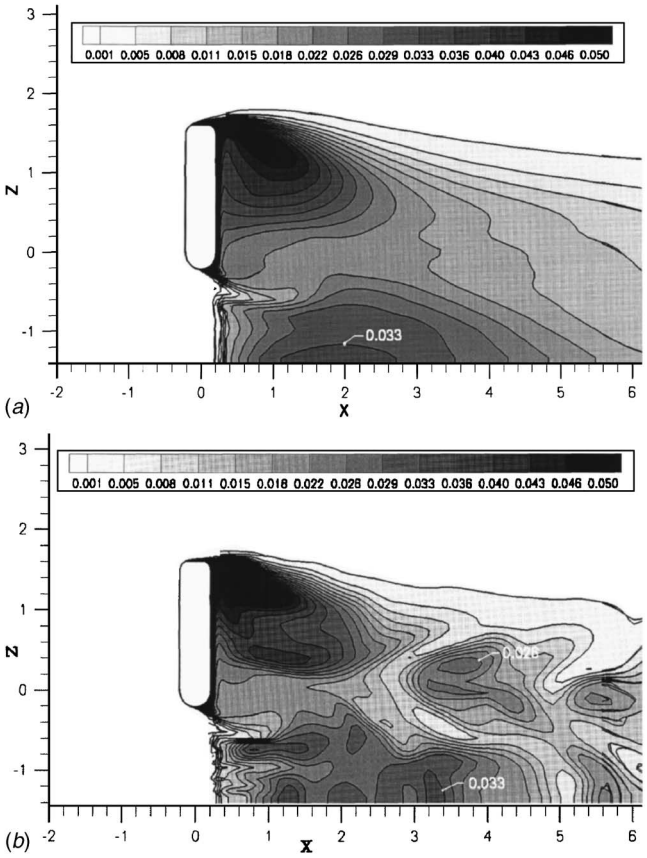

Fig. 19 Computed-mean (*a*) and instantaneous (*b*) scalar magnitude contours from a vertical slice through the centerline of the body

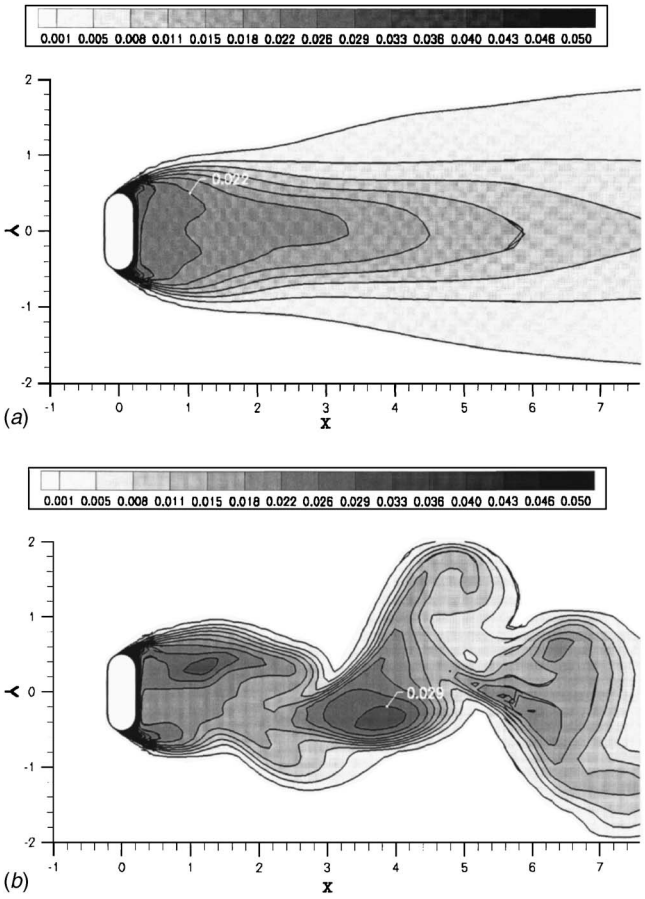

Fig. 20 Computed-mean (*a*) and instantaneous (*b*) scalar magnitude contours from a horizontal slice through the stomach

The grid study consists of three systematically refined grids where each successively refined grid reduces the mesh spacing by a factor of $\sqrt{2}$ in all directions. Comparing the results of the U velocity obtained from each grid, shown in Fig. 9, we see that similar results are obtained in the upper wake for all three grids and the solutions vary behind the lower wake, as anticipated. Although the solutions in the upper wake are similar, there is no consistency in the manner of convergence, i.e., the solutions converge in an oscillatory manner in some locations and in a monotonic fashion elsewhere. This is most likely due to the inclusion of the initial transient period in the time samples. While the results provide confidence that the grids are sufficiently refined to provide solutions to the governing equations, no quantitative estimates can be made regarding the magnitude of the numerical error. The computed-mean scalar concentration, shown in Fig. 10, leads to similar conclusions, except in the lower wake where the solutions are expected to differ. Although the sample size is not sufficiently large to obtain quantitative estimates of the numerical error, we feel confident in saying that the grids are sufficiently refined to provide plausible results for this problem.

While spatial discretizations account for part of the numerical error, temporal discretizations also contribute. Evaluation of these temporal contributions is performed through a time step study, the results of which are shown in Figs. 11 and 12. The nominal nondimensional time step size of 0.01 is represented by the dashed line and the finer time step size of 0.005 is shown in the solid line. While it is not possible to quantitatively evaluate convergence of the solutions, it is apparent from these figures that both solutions provide a similar estimate for the computed-mean velocity field, even in the lower wake region. The computed-mean scalar results also show good agreement.

Although a quantitative estimates of the numerical errors is not possible, these studies provide confidence that the medium grid resolution and finest time step size are appropriate choices for providing solutions to this problem. The solutions show convergence with grid refinement and little change is observed with the halving of the time step size.

7 Results and Conclusions

The numerical methods and grid presented in the previous sections are applied to two different cases of contaminant distribution at a single set of flow conditions as described in Sec. 3. The first part of this section will deal with the dynamics of the wake behind the human form and the second part will deal with transport of a scalar contaminant from the surface of the body. Two cases of contaminant distribution will be considered: a uniformly distributed contaminant over the entire surface of the body, and a localized patch of contaminant located on the frontal midriff of the body.

7.1 Fluid Dynamics. The fluid dynamics of the human wake are shown through plots of the velocity field. Figures 13–15 show contours of total velocity with tangential streamlines superimposed. The figures labeled as "*a*" show the computed-mean total velocity while the figures labeled as "*b*" show an instantaneous realization of the unsteady flow field. Figure 13 shows a slice of the flow field through the median plane of the body. This image shows a mean recirculation region in the upper wake (behind the torso) and a "jet" protruding from between the legs. The unsteady flow field also shows the recirculation zone, albeit with fluctuations in both the direction and magnitude of the velocity field. The recirculation region, as viewed from above, is shown in Fig. 14. This view represents a horizontal slice through the stomach at a constant elevation (i.e., Z=constant) and it confirms the existence

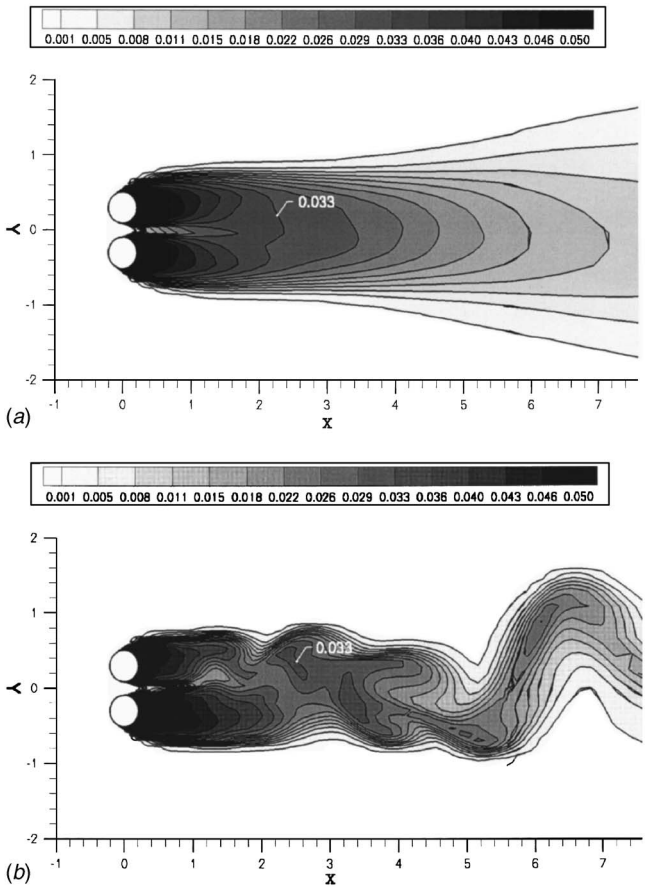

Fig. 21 Computed-mean (*a*) and instantaneous (*b*) scalar magnitude contours from a horizontal slice through the ankles

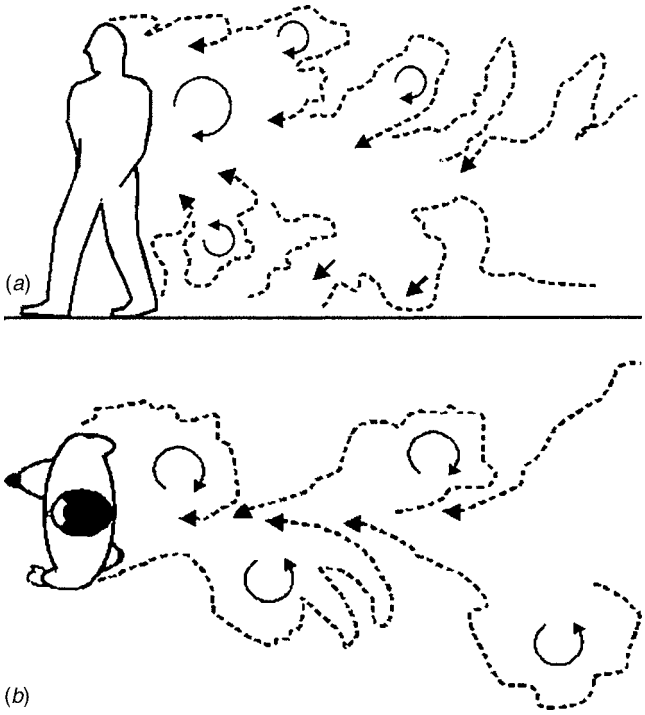

Fig. 22 Sketches of the significant physics observed in the flow visualization experiments performed by the Penn State Gas Dynamics Laboratory. (*a*) Vertical plane and (b) horizontal plane.

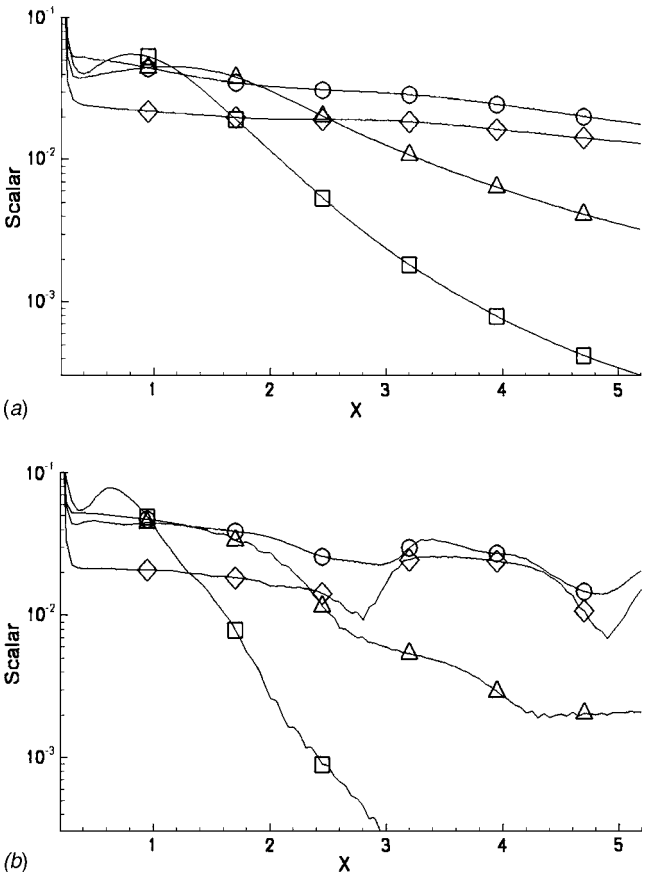

Fig. 23 Computed-mean (*a*) and instantaneous (*b*) scalar magnitude versus non-dimensional downstream distance *X* for the uniform contaminant source. Symbols define sample location: □ head, △ chest, ◇ stomach, and ○ feet.

of a mean recirculation region behind the torso. The instantaneous realization is considerably less symmetric, which suggests that the unsteady wake consists of asymmetric vortex shedding. Also note a large deviation in the wake velocity field 5 diameters downstream which indicates the existence of large-scale flow structures advecting downstream. The velocity field in the lower wake is presented in Fig. 15, which shows a horizontal slice through an elevation corresponding to the ankles. This figure clearly shows the "jet" between the legs with a magnitude that is roughly 30% greater than the free stream velocity. The computed-mean flow field (see the inset) shows the existence of a single recirculation in the wake region that is biased toward the outer side of the leg.

The vorticity within the wake region also provides some details of the wake dynamics. The instantaneous vorticity is presented in Figs. 16–18, with contours showing the magnitude of the out-of-plane vorticity. Figure 16, presenting the out-of-plane vorticity within the median plane, shows a strong negative vorticity concentration convecting off the head/shoulders and an even stronger vorticity concentration from the leg-body interface. Note that both vorticity concentrations follow the contour of the torso recirculation region and appear to be drawn downward as they are convected downstream. These observations, in conjunction with the observations of the velocity contours in Fig. 13, indicate the existence of a "downwash" behind the walking person in this Re regime.

Vorticity in the vertical direction ω_z is shown in Fig. 17, for the horizontal plane through the stomach. This plane shows the generation of strong vorticity regions along the side of the torso and the formation of left-right vortex shedding. Lateral spreading of the vorticity concentrations can be seen in the downstream wake (see the upper-right corner of Fig. 17). The lateral spreading is believed to occur by a combination of the asymmetric vortex

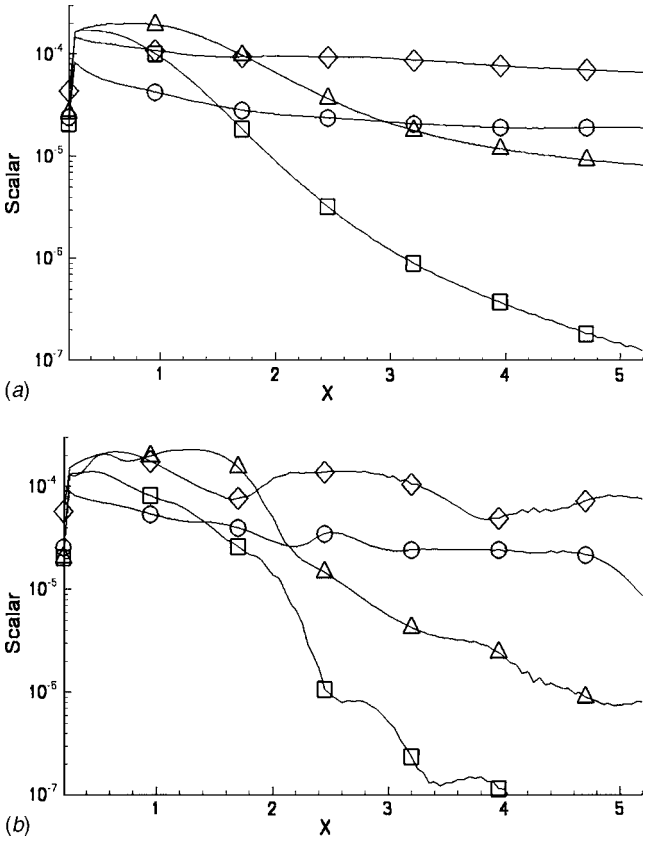

Fig. 24 Computed-mean (*a*) and instantaneous (*b*) scalar magnitude versus *X* for the localized contaminant source. Symbols define sample location: □ head, △ chest, ◇ stomach, and ○ feet.

shedding and the "downwash" noted earlier. The "downwash" causes lateral spreading as the fluid from the upper torso flows toward the ground where conservation of mass dictates that the lower wake region will expand. It should also be noted that the vortex in the upper right-hand corner corresponds with the large "hook" in the downstream wake of Fig. 14.

The vorticity in the lower wake behind the legs is presented in Fig. 18. The higher velocity of the "jet" tends to stretch the vorticity regions quite far when compared to the diameter of the legs before vortex shedding occurs two units downstream. Each leg appears to initiate left-right vortex shedding with the inner vortices quickly destroyed, leaving only the outer vortices to interact as vortex pairs. It is difficult to determine if the outer vortices pair in a symmetric or asymmetric manner.

7.2 Scalar Contaminant. The first contaminant boundary condition considered here consists of a uniform contaminant with a nondimensional magnitude of 1.0 over the entire surface of the body. The second boundary condition consists of a small localized patch of contaminant placed on the frontal midriff of the body.

The computed-mean and instantaneous contours of contaminant are shown in Figs. 19–21 for the first boundary condition. Figure 19 shows that the upper wake recirculation region contains higher levels of contaminant than the lower portion of the wake. This is a consequence of the surface area parallel to the flow on the shoulders and head. The lower portion of the recirculation region has much lower levels of contaminant due to the smaller surface between the legs which is the effective source of the contaminant.

A horizontal slice at the stomach is presented in Fig. 20. This figure shows the steady decay of the contaminant behind the body and the increased spreading of the wake around $X>2$. The increase in spreading of the contaminant is likely due to the combined effects of the left-right vortex shedding and the "downwash" effect. A horizontal slice through the ankles, Fig. 21, shows much higher concentrations of contaminant behind the legs, compared to the torso. This is due to the smaller recirculation zone and the increase in surface area supplying the contaminant. The computed-mean solution shows that the wake spreading does not become evident near the floor until $X>4$. The unsteady contaminant magnitudes seem to correlate well with the unsteady vorticity magnitudes of Fig. 18.

It is interesting to note that these computational results share many of the bulk flow structures that were observed in smoke visualization experiments performed at the Penn State Gas Dynamics Laboratory. Figure 22 shows artistic sketches of the bulk characteristics of the observed wake. The experiments showed considerable intermittency of the contaminant in the wake region and an observed lateral spreading of the wake around $X=3$ body widths downstream. These results are quite similar to the computational results depicted in Figs. 19 and 20.

The magnitude of the contaminant downstream of the body is shown in Figs. 23. It should be noted that the samples behind the ankle were taken directly behind the leg, not on the median plane of the flow. These figures highlight the exponential decay of the scalar quantity with downstream distance. This result is significant to applications that require sampling of the contaminant from the wake. The results imply that a sensor must be capable of detecting levels of the contaminant that are several orders of magnitude lower than the contaminant levels found at the surface of the body.

Results from the localized boundary condition are shown in Fig. 24. As we might expect from a drastically reduced surface area of the source, the contaminant magnitude in the wake is significantly lower than the levels observed in the previous case. From Fig. 24 we see that the exponential decay nature of the contaminant has not changed and its relative distribution throughout the wake remains surprisingly constant. This indicates that significant mixing is occurring between the various wake regions.

8 Summary and Recommendations

This paper has presented the results of an unsteady RANS simulation of the human aerodynamic wake and the transport of a scalar contaminant from the surface of the body. The results indicate the presence of a recirculation zone in the upper portion of the wake which persists from the head down to the legs. The recirculation region ends at the legs where it is broken up by the jet formed between the legs. The results also indicate a "downwash" that tends to spread the wake, and thus the contaminant, laterally behind the lower torso and legs.

Concentrations of a uniformly distributed contaminant within the wake are highest behind the shoulders and the legs. The higher concentrations correspond to locations where source areas are oriented parallel to the flow. Results of the localized contaminant show that the source location and size are important for determining the magnitude of the scalar throughout the wake, however, for the specific localized condition discussed here, these properties had little effect on the relative distribution of the contaminant.

Based on this work, several recommendations are provided for future studies. First, a wind tunnel experiment is currently in progress, the purpose of which is to acquire validation data. Near-term work should include comparing these experiments to the computational data with the goal of estimating model uncertainty. Second, a parametric study of walking speeds (i.e., Reynolds number), physiological body form, and clothing-related variability (i.e., robes and dresses) is recommended since these variables have potentially large impact on the wake dynamics.

Acknowledgment

This work was made possible by an Exploratory and Foundational grant from the Pennsylvania State University Applied Research Laboratory.

References

[1] Oertel, H., 1990, "Wakes Behind Blunt Bodies," Annu. Rev. Fluid Mech., **22**, pp. 539–564.

[2] Roshko, A., 1993, "Perspectives on Bluff Body Aerodynamics," J. Wind. Eng. Ind. Aerodyn., **49**, pp. 79–100.

[3] Williamson, C. H. K., 1996, "Vortex Dynamics in the Cylinder Wake," Annu. Rev. Fluid Mech., **28**, pp. 477–539.

[4] Okamoto, S., and Sunabashiri, Y., 1992, "Vortex Shedding from a Circular Cylinder of Finite Length Placed on a Ground Plane," ASME J. Fluids Eng., **114**, pp. 512–521.

[5] Park, C.-W., and Lee, S.-J., 2002, "Flow Structure Around a Finite Circular Cylinder Embedded in Various Atmospheric Boundary Layers," Fluid Dyn. Res., **30**, pp. 197–215.

[6] Park, C.-W., and Lee, S.-J., 2004, "Effects of Free-End Corner Shape on Flow Structure Around a Finite Cylinder," J. Fluids Struct., **19**, pp. 141–158.

[7] Song, C., and He, J., 1993, "Computation of Wind Flow Around a Tall Building and the Large-Scale Vortex Structure," J. Wind. Eng. Ind. Aerodyn., **46-47**, pp. 219–228.

[8] Sumner, D., Wong, S. S. T., Price, S. J., and Païdoussis, M. P., 1999, "Fluid Behaviour of Side-by-Side Circular Cylinders in Steady Cross-Flow," J. Fluids Struct. **13**, pp. 309–338.

[9] Meneghini, J. R., and Saltara, F., 2001, "Numerical Simulation of Flow Interference Between Two Circular Cylinders in Tandem and Side-by-Side Arrangements," J. Fluids Struct., **15**, pp. 327–350.

[10] Lewis, H. E., Foster, A. R., Mullan, B. J., Cox, R. N., and Clark, R. P., 1969, "Aerodynamics of the Human Microenvironment," Lancet, **322**(7609), pp. 1273–1277.

[11] Clark, R. P., and Cox, R. N., 1973, "The Generation of Aerosols from the Human Body," *Airborne Transmission and Airborne Infection: Concepts and Methods*, J. F. P. Hers and K. C. Winkler, eds., Wiley NY, pp. 413–426.

[12] Clark, R. P., and Edholm, O. G., 1985, *Man and his Thermal Environment*, E. Arnold, London.

[13] Gowadia, H., Strine, S., Johnson, T., and Settles, G., 1996. "The Natural Aerodynamic Sampling of Trace Explosives from the Human Body," *2nd FAA International Symposium on Explosives Detection Technology*, Atlantic City, NJ, Federal Aviation Administration, Washington, DC.

[14] Settles, G., and McGann, W., 2001, "Potential for Portal Detection of Human Chemical and Biological Contamination," *SPIE Aerosense Meeting*, Vol. 4394, paper 108, Orlando, FL, Society of Photo-Optical Instrumentation Engineers, Bellingham, WA.

[15] Settles, G., Ferree, H., Tronsky, M., Moyer, Z., and McGann, W., 2001. "Natural Aerodynamic Portal Sampling of Trace Explosives from the Human Body," *3rd International Symposium on Explosive Detection and Aviation Security*, Atlantic City, NJ, Federal Aviation Administration, Washington, DC.

[16] Gowadia, H., and Settles, G., 2001, "The Natural Sampling of Airborne Trace Signals from Explosives Concealed Upon the Human Body," J. Forensic Sci., **46**(6), pp. 1324–1331.

[17] Gowadia, H. A., 2000, "The Natural Sampling of Airborne Trace Signals Associated With the Human Body," Ph.D. thesis, The Pennsylvania State University.

[18] Homma, H., and Yakiyama, M., 1997, "Examination of Free Convection Around Occupant's Body Caused by it's Metabolic Heat," ASHRAE Trans., **103**(1), pp. 1–12.

[19] Murakami, S., Kato, S., and Zeng, J., 1997, "Flow and Temperature Fields Around Human Body with Various Room Air Distribution, CFD Study on Computational Thermal Manikin," ASHRAE Trans. **103**(1), pp. 1–12.

[20] Murakami, S., Zeng, J., and Hayashi, T., 1999, "CFD Analysis of Wind Environment Around a Human Body," J. Wind. Eng. Ind. Aerodyn., **83**, pp. 393–408.

[21] Rodel, C. E., Kamens, R. M., and Wiener, R. W., 1995, "Experimental Considerations for the Study of Contaminant Dispersion Near the Body," Am. Ind. Hyg. Assoc. J. **56**(6), pp. 535–545.

[22] Kim, T., and Flynn, M. R., 1991, "Airflow Pattern Around a Worker in a Uniform Freestream," Am. Ind. Hyg. Assoc. J. **52**(7), pp. 287–296.

[23] Flynn, M. R., and Miller, C. T., 1991, "Discreet Vortex Methods for the Simulation of Boundary-Layer Separation Effects on Worker Exposure," Ukr. J. Phys. **35**(1), pp. 35–50.

[24] Moyer, Z. M., 2003, The Human Aerodynamic Wake and the Design of a Portal to Sample It, Master's thesis, The Pennsylvania State University.

[25] Menter, F. R., 1994, "Two-equation eddy-viscosity turbulence models for engineering applications," AIAA J. **32**(8), pp. 1598–1605.

[26] Paterson, E. G., Wilson, R. V., and Stern, F., 2003, "General-Purpose Parallel Unsteady RANS Ship Hydrodynamics Code: CFDSHIP-IOWA, Technical Report 432, Iowa Institute of Hydraulic Research, April.

[27] Issa, R. I., 1985, "Solution of the Implicitly Discretized Fluid Flow Equations by Operator-Splitting," J. Comput. Phys. **62**, pp. 40–65.

[28] Edge, B., Trujillo, M., Paterson, E., and Peltier, L. J., 2004, "Prediction of Forces and Moments on a Sonobuoy Configuration Using Overset Grids and DES." *7th Overset Composite Grid and Solution Technology Symposium*, Huntington Beach, CA, The Boeing Company, Huntington Beach, CA.

[29] Paterson, E., and Peltier, L. J., 2004, Detached-eddy simulation of high Reynolds number trailing-edge flows and wakes, *Symposium on LES Advancements and Applications, ASME FED Summer Meeting*, Charlotte, NC, American Society of Mechanical Engineers, Fluids Engineering Division, New York, NY.

[30] Paterson, E., Poremba, J., Peltier, L. J., and Hambric, S., 2004, "A Physics-Based Simulation Methodology for Predicting Trailing-Edge Singing," *25th Symposium Naval Hydrodynamics*, St. Johns, Newfoundland and Labrador, Canada, Office of Naval Research, Washington, DC.

[31] Meyer, R., Zajackowski, F., Straka, W., Paterson, E.2004, "Experimental and Computational Study of Cavitation Inception in Co-Flow Nozzles, *25th Symposium Naval Hydrodynamics*, St. Johns, Newfoundland and Labrador, Canada, Office of Naval Research, Washington, DC.

[32] Paterson, E., and Baker, W., 2004, "Simulation of Steady and Pulsed Circulation Control for Marine-Vehicle Control Surfaces, *42nd AIAA Aerospace Sciences Meeting*, Reno, NV, American Institute of Aeronautics and Astronautics, Reston, VA.

[33] Suhs, N. E., Rogers, S. E., and Dietz, W. E., 2002. "Pegasus 5: An automated pre-processor for overset grid CFD," *32nd AIAA Fluid Dynamics Conference, AIAA 2002-3186*, St. Louis, MO, American Institute of Aeronautics and Astronautics, Reston, VA.

[34] Chan, W. M., III, Gomez, R. J. , Rogers, S. E., and Buning, P. G., 2002, "Best Practices in Overset Grid Generation," *32nd AIAA Fluid Dynamics Conference, AIAA 2002-3191*, St. Louis, MO, American Institute of Aeronautics and Astronautics, Reston, VA.

[35] Pope, S. B., 2000, *Turbulent Flows*, Cambridge University Press, Cambridge, England.